



**HAL**  
open science

## Two-phase damping for internal flow: Physical mechanism and effect of excitation parameters

C Charreton, Cédric Béguin, A Ross, Stéphane Etienne, M.J. Pettigrew

### ► To cite this version:

C Charreton, Cédric Béguin, A Ross, Stéphane Etienne, M.J. Pettigrew. Two-phase damping for internal flow: Physical mechanism and effect of excitation parameters. *Journal of Fluids and Structures*, 2015, 56, pp.56-74. 10.1016/j.jfluidstructs.2015.03.022 . hal-01223577

**HAL Id: hal-01223577**

**<https://hal.science/hal-01223577>**

Submitted on 2 Nov 2015

**HAL** is a multi-disciplinary open access archive for the deposit and dissemination of scientific research documents, whether they are published or not. The documents may come from teaching and research institutions in France or abroad, or from public or private research centers.

L'archive ouverte pluridisciplinaire **HAL**, est destinée au dépôt et à la diffusion de documents scientifiques de niveau recherche, publiés ou non, émanant des établissements d'enseignement et de recherche français ou étrangers, des laboratoires publics ou privés.

# Two-phase damping for internal flow : physical mechanism and effect of excitation parameters

C. Charreton, C. Béguin, A. Ross, S. Étienne, M.J. Pettigrew

## Abstract

Two-phase flow induced-vibration is a major concern for the nuclear industry. This paper provides experimental data on two-phase damping that is crucial to predict vibration effects in steam generators. An original test section consisting of a tube subjected to internal two-phase flow was built. The tube is supported by linear bearings and compression springs allowing it to slide in the direction transverse to the flow. An excitation system provides external sinusoidal force. The frequency and magnitude of the force are controlled through extension springs. Damping is extracted from the frequency response function of the system. It is found that two-phase damping depends on flow pattern and is fairly proportional to volumetric fraction for bubbly flow. Measurements are completed by the processing of high-speed videos which allow to characterize the transverse relative motion of the gas phase with respect to the tube for bubbly flow. It is shown that the bubble drag forces play a significant role in the dissipation mechanism of two-phase damping.

## Keywords

Two-phase, damping, flow pattern, bubble motion

Department of Mechanical Engineering, École Polytechnique de Montréal, P.O. Box 6079, Succ. Centre-Ville, Montréal, Québec, Canada H3C 3A7

# Amortissement diphasique pour un écoulement interne : mécanisme physique et effet des paramètres d'excitation

C. Charreton, C. Béguin, A. Ross, S. Étienne, M.J. Pettigrew

## Résumé

Les vibrations induites par les écoulements diphasiques sont une préoccupation majeure pour l'industrie nucléaire. Cet article présente des expériences de mesure de l'amortissement diphasique. La connaissance de l'amortissement diphasique est cruciale pour prédire les vibrations dans les générateurs de vapeur. Une section d'essai composée d'un tube de section carré soumis à écoulement interne diphasique a été construite. Le tube est soutenu par des roulements linéaires et des ressorts de compression lui permettant de se déplacer dans la direction transversale à l'écoulement. Un système d'excitation fournit une force sinusoïdale externe. La fréquence et l'amplitude de la force excitatrice sont contrôlées par des ressorts d'extension. L'amortissement est extrait de la fonction de transfert du système. Il est constaté que l'amortissement diphasique dépend du régime d'écoulement. Pour un écoulement à bulles, l'amortissement diphasique est quasiment proportionnel à la qualité volumétrique. De plus un traitement des vidéos à haute vitesse ont permis de caractériser le mouvement relatif transversale de la phase gazeuse par rapport au tube pour un écoulement à bulles. Il est montré que la trainée de la bulle joue un rôle essentiel dans le mécanisme de l'amortissement diphasique.

## Mots-clés

diphasique, amortissement, régime d'écoulement, mouvement de bulle

Département de génie mécanique, École Polytechnique de Montréal, P.O. Box 6079, Succ. Centre-Ville, Montréal, Québec, Canada H3C 3A7

## 1. Introduction

Two-phase flow induced vibration in steam generators is well documented in the literature ([1], [2], [3]). Extensive experimentations have been carried out over the last forty years to get a better hand on the several excitation mechanisms involved, such as quasi-periodic forces or fluidelastic instability. Review and design guidelines for heat exchangers constructors have been proposed, improving nuclear power plant safety and reliability. The duality of two-phase flows from a vibration point-of-view lies in the fact that they bring about destructive phenomena while causing significant damping on the structure. Damping is a crucial input parameter to predict vibration effects in steam generators. However, the nature of the damping is not well understood. A better knowledge of the physical mechanism involved would lead to improved modeling of vibration effects in the near future.

The first experimental studies on two-phase damping were performed by [4] and [5]. For a cylinder confined in axial two-phase flow, they found that total damping is strongly dependent on void fraction. Moreover, the two-phase damping component is much higher than the damping due to fluid viscosity for single-phase flow. It can reach up to 3%. [6] derived an analytical model for a cylinder confined in axial-two-phase flow. They modeled the gas phase as columns having no mass nor stiffness. Cylinder and gas motions were described by beam equations, coupled by the fluid forces. Coupling coefficients were extracted from potential flow theory. The eigenvalue problem was solved to find the damping coefficients which compared well with the experiments. However, this approach does not provide a physical explanation for the mechanism. More recently, [7] proposed a numerical simulation, also for a cylinder confined in two-phase flow, assuming a bubbly flow. Damping values of the same order of magnitude as in [5] were observed. However, the damping ratio goes down to zero for void fractions higher than 60%, which is not verified experimentally. This fact raises questions about the applicability of numerical codes for high void fraction. Indeed, these codes assume bubbly flow but usually do not take flow pattern transitions into account. Nevertheless, [7] explains damping by “the phase lag of the drag force acting on the cylinder behind the cylinder displacement”. This introduces a notion of relative displacement inherent to the two-phase mixture.

Two-phase damping has also been measured for cross-flow. It is undoubtedly the most important flow configuration since most vibration mechanisms are critical in the U-bend region of the steam generator. Semi-empirical relations for design purposes are given by [8]. They compiled a considerable amount of data to identify the most influent parameters. It was shown that flow velocity and tube frequency have minor influence, contrary to confinement and surface tension. Therefore, several phenomena are potential dissipative mechanisms that could be responsible for two-phase damping. Mainly, flow structure, relative motion of gas phase and liquid phase and coalescence/breakup of bubbles are suspected.

Other studies were steered towards the influence of fluid properties on two-phase damping at Ecole Polytechnique of Montreal. These were performed for internal axial flow on clamped-clamped tubes. This configuration is less interesting from a practical point-of-view since in CANDU nuclear plants, pressurized heavy water is supposed to be almost liquid inside steam generator tubes. Still, it is interesting to notice that two-phase damping vs void fraction curves are oddly the same for the three flow configurations reported : annular, internal axial and cross-flow (see [5], [9] and [8] respectively). This suggests that the mechanism involved is the same for each case. From a design point-of-view, internal axial flow configuration is the simplest. [9] reported damping measurements in 20 mm tubes. The decrease of two-phase damping at the transition between bubbly and slug flow is explained by the decrease of interface surface area when slugs appear. This is somehow contradictory with Pettigrew’s observations:  $\zeta$  was found to increase with surface tension  $\sigma$ . A possible explanation given was that bigger bubbles are more prompt to dissipate energy. This work was pursued by [10] who tested several air-liquid mixtures, in order to assess the effect of viscosity and density on two-phase damping. [11] also performed two-phase damping experiments with rigid spheres in sedimentation in stagnant liquids. It appeared that density difference between phases has a major effect, contrary to the viscosity. Damping values with rigid spheres were somehow smaller than in air-liquid mixtures by a factor 2, but proportionality with respect to interface surface area was confirmed. For large number of spheres, interaction occurring between spheres (*e.g.* onset of coalescence in case of a gas phase) seems to modify this trend. [11] also presented a 2D model of a bubble in an oscillating tube filled with liquid, and solved the Navier-Stokes equations analytically. They showed that viscous dissipation due to the presence of a bubble can be related to the relative motion of the bubble with respect to the structure.

These conclusions motivated the design of a new test section which would not only allow damping measurements but also let us observe the gas phase behavior. Also, damping values have

only been extracted at the natural frequency of the considered system so far. Thus, the objective of this project is to measure two-phase damping accurately, so as to relate it to the relative motion of the gas phase that we also measured.

In the next section, a new test rig is presented. It allows to command excitation parameters, such as frequency, on a structure subjected to internal two-phase flow. This leads to interesting information on the nature of the two-phase flow energy dissipation. Then, the experimental parameters involved in the system are described. In 4, the technique to extract the two-phase damping component of the oscillating structure is presented. Results on damping and the relation with flow patterns are described afterwards. Then, in 6, the motion of the gas phase is characterized with the processing of high-speed videos. It is related to the two-phase values through an analytical model of the forces exerting on the bubbles in 7.

## 2. Experimental setup

The experimental setup is comprised of several features that will be described separately for the sake of clarity.

**Sliding tube:** The section itself is a stiff aluminum square tube. The hydraulic diameter  $D_h$  is 76.2 mm and the length  $L$  is 1 m. It is vertically mounted and supported by four linear bearings installed on two parallel shafts. This feature allows the tube assembly to slide in the  $y$ -direction only, transverse to the flow (cf. 1). The linear bearings are self-aligning to minimize friction in the system. Three panels of the tube are transparent, and the square section prevents refraction effects, allowing a good visualization of the flow.

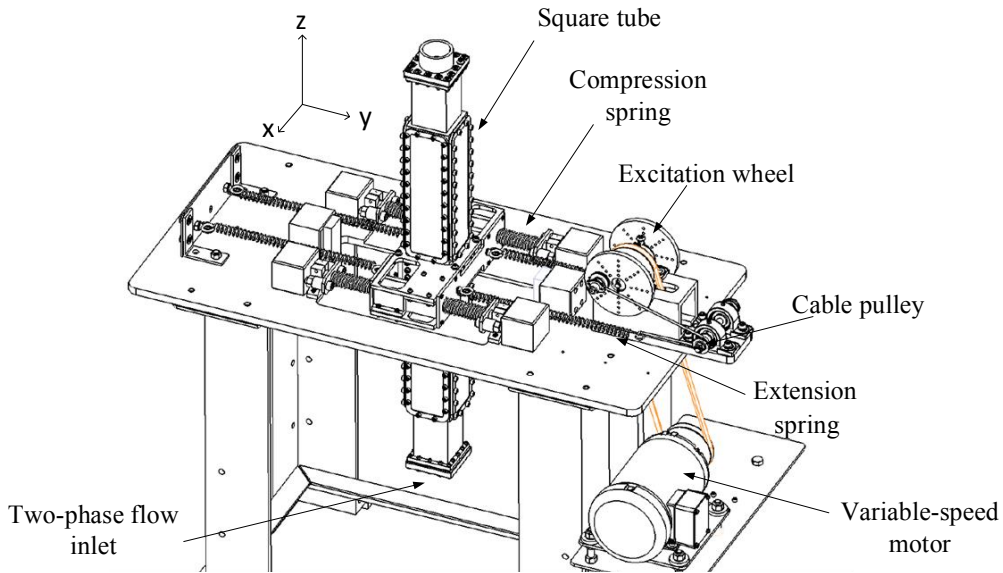


Figure 1. Test section (pipe system not shown).

**Compression system:** Four compression springs of stiffness  $k_c$  and concentric with the rods retain the test section in the  $y$ -direction. One of their ends is in contact with the tube assembly and the other with what we refer to as compression plates. These are bolted with the sturdy bench structure via threaded rods (see 2). They can be displaced along those threaded rods to set an initial compression to the springs. This is an important feature since it prevents the tube assembly from impacting the two sets of springs when oscillating. The four springs are always working. However, the maximum amplitude that the system can reach is equal to the length of the initial compression. Beyond that point, the tube assembly would disconnect from a pair of springs. The compression springs used in the present study have a free length of 152 mm and the initial compression is 45 mm. The tube assembly behaves like a classic mass-spring system, from a structural point-of-view.

**Excitation system:** The “mass-spring system” is forced with a simulated sinusoidal excitation, provided through extension springs of stiffness  $k_0$ . A motor drives an excitation wheel (cf. 1) via a pulley. A cable is attached to a shoulder-bearing system screwed eccentrically on the excitation wheel. The rotary motion is converted via the cable-pulley system into a sinusoidal motion of the extremity of extension springs (cf. 1). Since the extension springs are always stretched, the tube undergoes a sinusoidal force. We can control its magnitude  $F_0$  by changing the eccentricity  $e$  on the

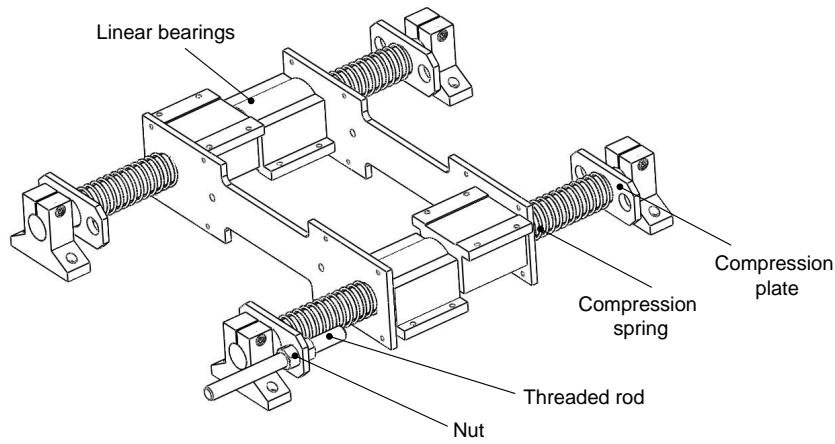


Figure 2. Sliding system.

excitation wheel. The latter is drilled with multiple tapped holes at different positions. The excitation frequency  $\omega$  can be changed using the variable-frequency drive that pilots the motor.

Notice the symmetry of the system with respect to the  $yz$ -plane: it is excited through two springs. Two additional extension springs are supporting the tube on the left side of the bench on 1, to ensure symmetry with respect  $xz$ -plane. All the springs, including compression springs, were tested on a traction-compression machine in order to verify their linearity over their range of operation. Dynamic stiffnesses have not been tested but are neglected since the excitation frequencies are very low (around 6Hz).

**Hydraulic loop:** In order to allow the transverse motion of the oscillating tube under internal flow, we use two flexible hoses that are fitted on both ends of the tube, and to the rest of the rigid pipe system on the other end. The flexible hoses are corrugated to ensure local pressure resistance and global flexibility, so as to not affect the tube motion. Also, their lengths were chosen so as to avoid an unbalancing mass effect at mid-section induced by water presence and make sure that they “follow” the tube smoothly.

The hydraulic loop works as follows: a centrifugal pump takes water from a reservoir. Air is injected just upstream the test section, as illustrated in 3. A mixer placed in the circular to square expansion homogenizes the air-water mixture. The mixture flows upward through the test section and then back to the tank at atmospheric pressure, where the phases separate.

**Measurement system:** The position of the tube is measured in time with laser sensors. They yield a resolution lower than  $12 \mu\text{m}$ . The acquisitions are performed at a sampling rate of 2048 Hz.

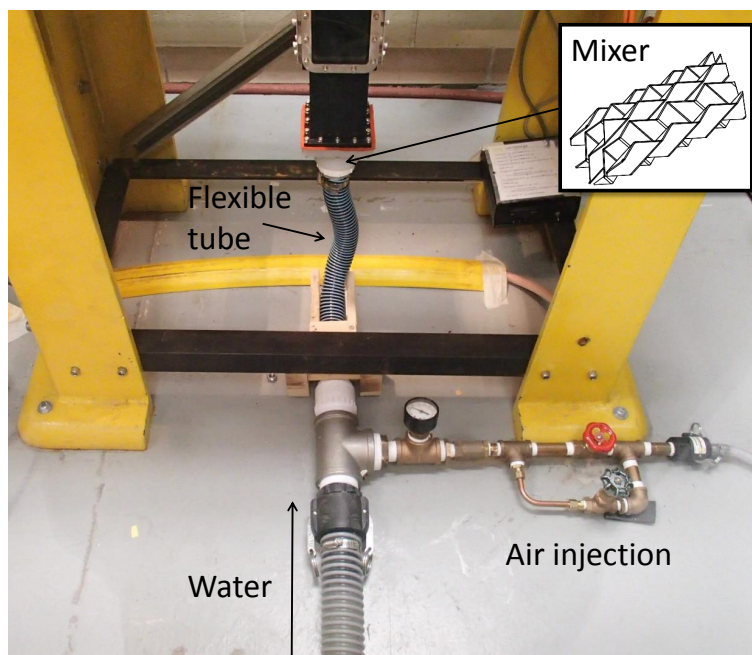


Figure 3. Air injection upstream to the test section.

Key parameters of the system are highlighted in Tab. 1.

**Table 1.** Characteristics of the system.

Property	Notation	Value/Range
Hydraulic diameter	$D_h$	76.2 mm
Tube area	$A$	$D_h \times D_h$ (square tube)
Tube length	$L$	1 m
Mass of tube assembly <sup>2</sup>	$m_s$	17 kg
Compression spring constant <sup>1</sup>	$k_c$	6545 N/m
Extension spring constant <sup>1</sup>	$k_0$	474 N/m
Natural frequency	$f_n$	6.45 Hz
Excitation force	$F_0$	23 - 69 N

<sup>1</sup> Average of measured values over the four springs.

<sup>2</sup> Calculated with 12 for the empty tube.

### 3. Experimental parameters

#### 3.1 Two-phase flow parameters

Two-phase flow in a tube can be characterized either by the void fraction  $\varepsilon$  in a portion  $\Delta L$  or by the volumetric fraction  $\beta$  [[12]]. The void fraction represents the proportion of gas volume over the total volume:

$$\varepsilon = \frac{V_g}{V_g + V_l} = \frac{A_g \Delta L}{A_g \Delta L + A_l \Delta L} = \frac{A_g}{A_g + A_l} \quad (1)$$

where  $A_k$  is the area occupied by phase  $k$  in a given section of the tube. The void fraction would require specific instrumentation such as capacitance or fiber optic probes to be accurately determined. On the other hand, the volumetric fraction only requires the volume flow rates of each phase:

$$\beta = \frac{Q_g}{Q_g + Q_l} = \frac{A_g \langle u_g \rangle}{A_g \langle u_g \rangle + A_l \langle u_l \rangle} = \frac{A_g}{A_g + A_l/s} \quad (2)$$

The volume and area void fractions are equal for fully developed two-phase flows. where  $s$  is the slip ratio between the average velocities of the phases:  $s = \langle u_g \rangle / \langle u_l \rangle$ . Note that  $\varepsilon = \beta$  if  $s = 1$ , which is the definition of a homogeneous flow.

We characterize the mixture velocity using the definition of superficial velocity:

$$j = \frac{Q_g + Q_l}{A} \quad (3)$$

The experiments were performed at constant  $j$ , using the fact that  $j_g = \beta j$  and  $j_l = (1 - \beta)j$ . Volumetric flow rates are both measured with appropriate flow meters.

#### 3.2 Sources of damping

The presence of fluid around a structure will affect its damping. [5] identified several sources of damping:

$$\zeta_t = \zeta_s + \zeta_f + \zeta_\nu + \zeta_{2\varphi} \quad (4)$$

- (i)  $\zeta_s$  : **Structural** damping is caused by the energy losses inherent to the motion of a structure. In our case, it is due to the friction in the linear bearings and inner losses in the springs. Its value is obtained by determining the oscillating characteristics of the system while no fluid is flowing through ( $j = 0$ ).
- (ii)  $\zeta_f$  : When water is flowing through a slender pipe, the latter can warp and oscillate under fluid force. This force causes a damping effect at the elbows: it is the **fluid** damping mechanism. Since our structure is practically stiff,  $\zeta_f$  can be neglected.

- (iii)  $\zeta_\nu$  : Fluid friction on the sides of the test section induces **viscous** damping, which depends on fluid properties, fluid velocity and channel geometry. As can be seen on 4, it is negligible at 100% void fraction, and is monotonic until 0% (water only). Even there,  $\zeta_\nu$  is small compared to  $\zeta_{2\phi}$ . We determine  $\zeta_\nu$  at  $\varepsilon = 0\%$ . Then, it is assumed that  $\zeta_\nu$  decreases linearly with  $\varepsilon$  and is null at  $\varepsilon = 100\%$  for a given superficial velocity of the mixture.
- (iv)  $\zeta_{2\phi}$  : The **two-phase** component is obtained by subtracting the aforementioned components from the measured total damping  $\zeta_t$ .

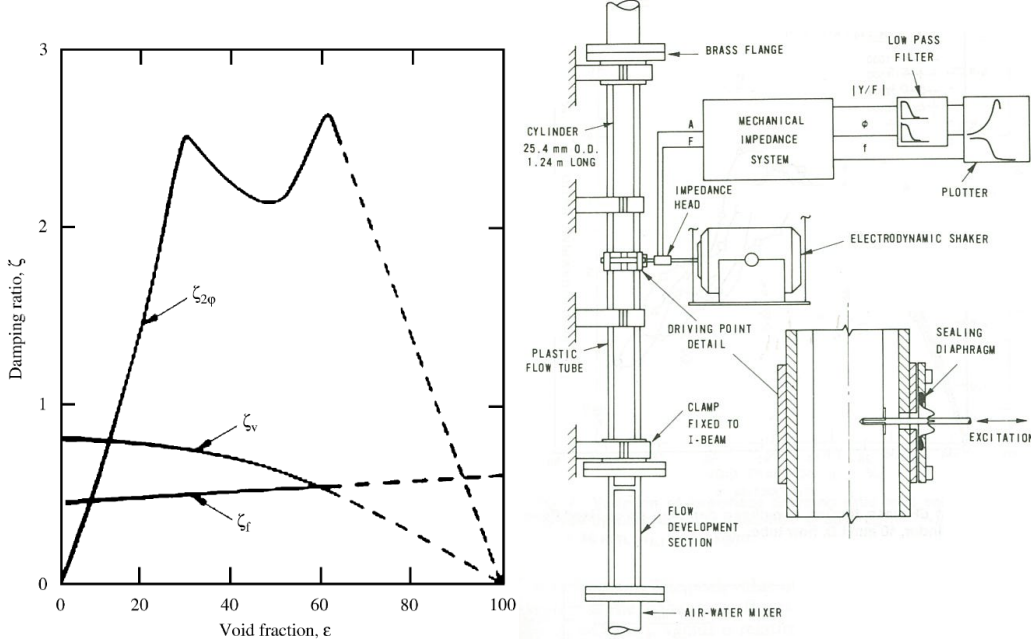


**Figure 4.** Components of total damping in two-phase axial flow and experimental apparatus. Total and structural damping are measured, fluid and viscous damping modeled [4].

This formulation suggests that all the components are purely velocity dependent. This is not the case for this system, as dry friction occurs in the linear bearings. 4 aims at describing how the two-phase component is therefore extracted.

## 4. Experimental technique

### 4.1 Structural damping

Information on the nature of structural damping is determined by analyzing the free vibrations of the system. The empty tube was initially displaced by 20 mm and then released. The result is shown on 5. The linear envelope is typical of Coulomb friction, occurring in the linear bearings. It is explained by the fact that a constant amount of energy is extracted from the system at each cycle, meaning that it is not velocity dependent. Since in this case, we know the weight of the tube assembly, we can calculate a friction coefficient  $\mu$  of 0.06 per bearing. This value is inside the expected range [0.04, 0.07] for linear bearings [[13]], where friction is indubitably higher than in roller bearings. In order to test the effect of mass and frequency, the tube assembly was ballasted with several masses or stagnant water, and different springs were used. As a result, total mass  $m$  over structural mass  $m_s$  was varied within [1, 1.6] and natural frequency within [10, 30] rad/s. Coulomb friction coefficient was found to vary within [0.04, 0.08].

In theory, pure Coulomb friction allows an infinite response at resonance for a mass-spring system, for low values of  $\mu$  such as in our case [[14]]. Therefore, a combination of Coulomb friction and viscous damping is commonly used. A more elaborate friction model [[15]] did not prove to be necessary, as the tube is constantly sliding (no stick-slip phenomena, for instance, are involved). We then introduce  $\zeta_s$ , the viscous component due to structural losses. The determination of  $\mu$  and  $\zeta_s$ , along with the other sources of damping, requires an appropriate modeling of the system for operating conditions.

### 4.2 System modeling

A top view of the test section is provided on Fig. 6(a). We can identify the four compression springs and the two pairs of extension springs, clamped on the right hand side and excited on the left hand

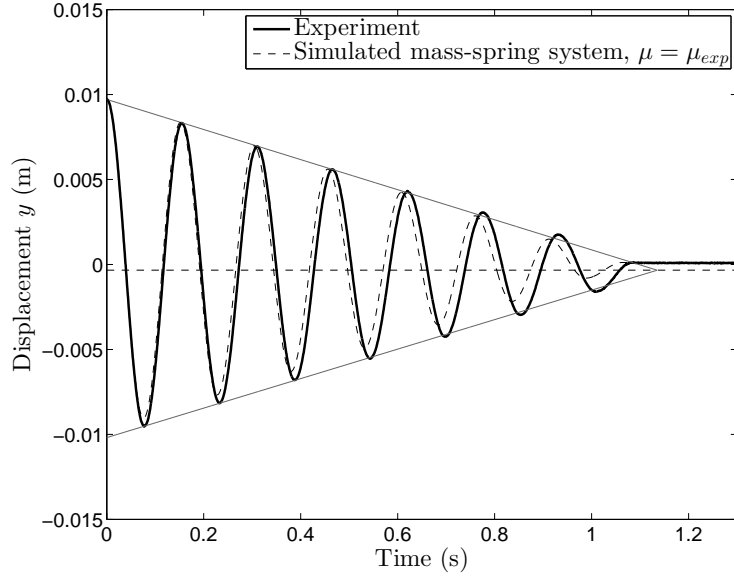


**Figure 5.** Free response of the empty tube after an initial displacement.

side.

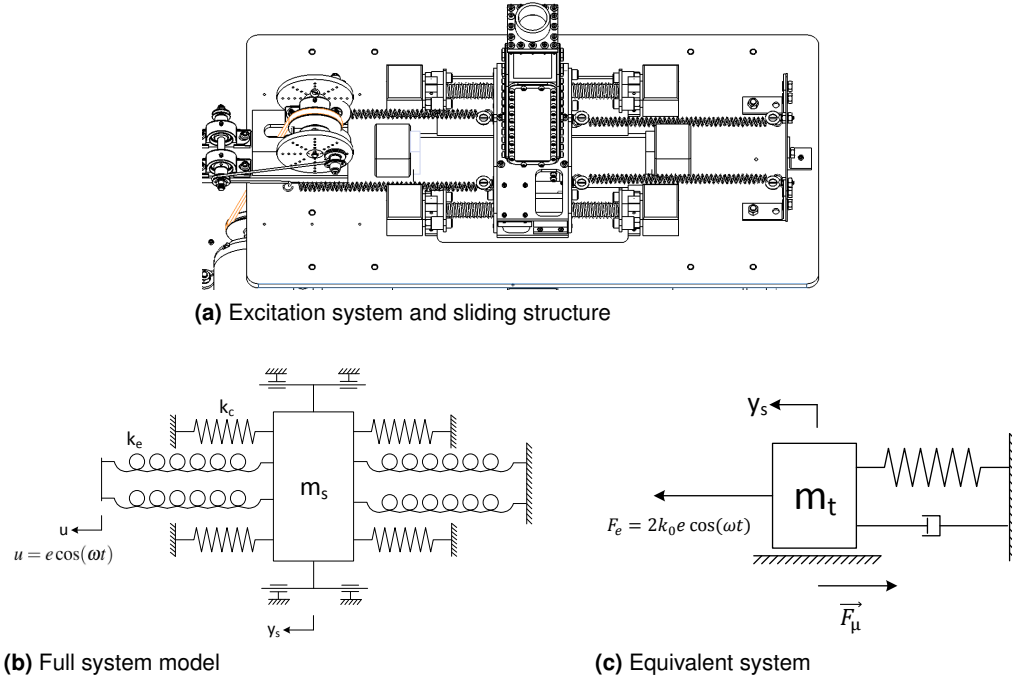


**Figure 6.** System modeling.

6(b) shows the full system model from a structural point-of-view. The mass of the tube assembly is noted  $m_s$  and its position  $y_s$ . The springs are considered to be linear, based on the traction-compression tests mentioned earlier in this paper. The excitation springs are subject to a sinusoidal displacement. We isolate the forces (including the different sources of damping and friction) on the free body diagram of the tube assembly. Remembering that because of the initial compression, all the springs are always working, the equivalent variables of the system under operating conditions (6(c)) are:

$$\text{Force magnitude} : F_0 = 2k_0e \quad (5)$$

$$\text{Stiffness} : k_t = 4k_0 + 4k_c \quad (6)$$

$$\text{Damping} : c_t = c_s + c_\nu + c_{2\varphi} \quad (7)$$

$$\text{Mass} : m_t = m_s + m_{2\varphi} + m_a \quad (8)$$

The total damping coefficient  $c_t$  is the sum of the three aforementioned components.  $m_{2\varphi}$  is the

mass of fluid vibrating with the structure and can be deduced from  $\varepsilon$  and tube geometry.  $m_a$  is the added mass, due to a relative motion between the liquid and the structure. The equation of motion of the structure in direction  $y$ , for a given excitation frequency  $\omega$ , is:

$$m_t \ddot{y}_s + c_t \dot{y}_s + k_t y_s = F_\mu(\dot{y}_s) + F_e(t) \quad (9)$$

$$= -\mu m_t g \operatorname{sgn}(\dot{y}_s) + 2k_0 e \cos(\omega t) \quad (10)$$

It can be rewritten as:

$$\ddot{y}_s + 2\zeta_t \omega_n \dot{y}_s + \omega_n^2 y_s = -\mu g \operatorname{sgn}(\dot{y}_s) + \frac{2k_0 e \omega_n}{k_t} \cos(\omega t) \quad (11)$$

with the damping ratio  $\zeta_t$  and the natural frequency  $\omega_n$  defined as usual as:

$$\zeta_t = \frac{c_t}{2\sqrt{k_t m_t}} \text{ and } \omega_n = \sqrt{\frac{k_t}{m_t}} \quad (12)$$

The total damping ratio is non-dimensionalized by the total mass, including the added mass. In this case, the added mass is negligible compared to  $m_s$  and  $m_{2\varphi}$ . The relative error is estimated to be lower than 3% on  $\zeta_t$ .

11 is non-linear because of the friction force. Thus, finding an analytical expression for  $\zeta_t$  is far from straightforward. The next paragraph describes the method to retrieve variables of 12 from the frequency response function of the system.

### 4.3 Protocol

The position of the tube is acquired with the laser sensors. The time domain samples have a duration of 20 seconds. A typical tube response is shown on 7. The RMS amplitudes of tube  $Y_s^{rms}$  and excitation frequencies  $\omega$  are extracted from these samples.

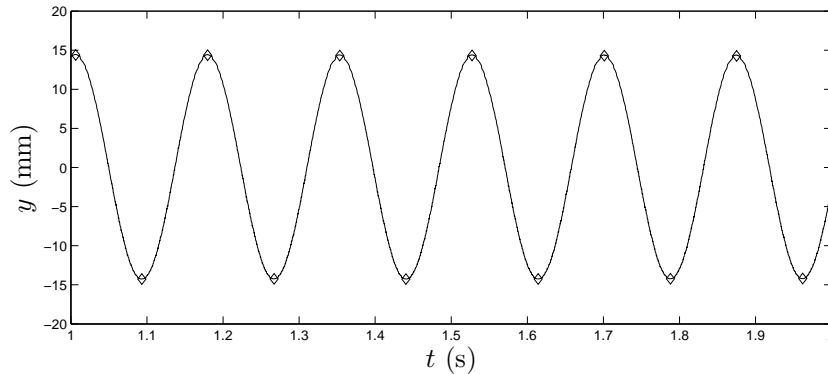
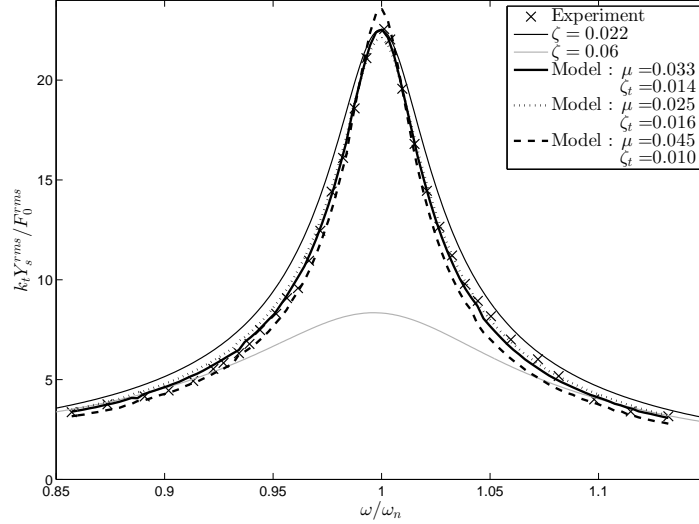


Figure 7. Measured position signal of the tube.

This operation is repeated by increasing  $\omega$  with the variable frequency drive in order to cover the resonance peak of the structure in the frequency spectrum. The frequency resolution that we get on the tube (including power transmission ratios) is 0.03 Hz. This frequency sweep allows to construct the frequency response function of the tube, as illustrated on Fig 8.

The black and gray curves calculated for a linear system ( $\zeta = 2.2\%$  and  $\zeta = 6.0\%$  respectively) have been overlaid to illustrate the slight non-linearity of the system. Around resonance, the experimental points are closer to the black curve whereas when excited farther away from the natural frequency, they are closer to the grey curve.

The natural frequency of the system is extracted from a polynomial fit around the resonance point. Then, we use the least-squares method to find values for  $\mu$  and  $\zeta_t$  of 11. Indeed, we do not know the weight supported by the bearings when there is flow. The bottom flexible tube may pull the tube assembly down whereas the flow going up might reduce the force on the bearings. Since the peak of resonance is well defined ( $\zeta_t$  is expected to be smaller than 6%), only a narrow range of excitation frequency is required to accurately determine the damping. Therefore, we consider  $\mu$  to be constant over a frequency response function for given conditions. So, 11 is solved for all the frequencies tested, the RMS amplitudes are calculated and compared with the experimental values.  $\mu$  and  $\zeta_t$  are found to best fit the experimental data in the frequency domain. The result is summarized by the dotted line on Fig 8.



**Figure 8.** Frequency response function of the system ( $F_0 = 23$  N,  $j = 0.7$  m/s,  $\beta = 30\%$ ).

Note on 10 that the model suggests that the total mass  $m_t$  is supported by the bearings. Since a smaller value for the mass is expected in reality (as explained in the previous paragraph), the compensation is done directly on the friction coefficient. The values of  $\mu$  for the conditions tested lie within  $[0.025, 0.045]$ , just below the range expected from the free vibration tests, where the total mass of the system was supported by the bearings in this case. For the experiments with two-phase flow, where the reaction supported by the bearings is unknown, the parameter  $\mu$  should be interpreted as the ratio of friction forces on the overestimated reaction  $= f_\mu / (m_t g)$ . In fact, the values of  $\mu$  vary depending on the flow conditions. For the case presented on Fig. 7, if we force  $\mu$  rather than fitting it, we obtain  $\zeta_t = 1.6\%$  underestimating the friction force with  $\mu = 0.025$  and  $\zeta_t = 1\%$  overestimating the friction force with  $\mu = 0.045$  presented in dotted and dashed line. The best fit is  $\zeta_t = 1.4\%$  for  $\mu = 0.033$  closest to the experimental condition. We can therefore estimated the absolute experimental error as  $\pm 0.3\%$

This confirms that the non-linearity of the system can be explained by Coulomb friction induced by the bearings only. Furthermore, the good agreement between the model and experiments shows that two-phase damping can be modeled as a velocity dependent damping.

## 5. Results

### 5.1 Influence of fluid velocity

Total damping results are shown on Fig. 9 as function of volumetric fraction  $\beta$ , for the three superficial velocities of the mixture tested. Each point is the average over three measurements. First-of-all, we can see for  $\beta = 0\%$  that  $\zeta_s + \zeta_\nu$  is fairly small, of the order of 0.5 to 1%. Then, damping seems proportional to volumetric fraction until a change in slope occurs (vertical dashed line). This transition corresponds to the transition between bubbly and churn regimes, as will be discussed in 5.2. The breakdown in damping values was related to the change in interface surface area by [9]. As anticipated, the two-phase damping values are very high and reach 3%. However, damping is expected to go down for high volumetric fraction, since the flow becomes air single-phase. This behavior can be explained with 10.

10 shows the evolution of the natural frequency of the system. When  $\beta$  is increased, the mass of the vibrating fluid decreases. Thus, the natural frequency of the total system increases. The dotted line represents the expected natural frequency in the context of a perfectly homogeneous flow, neglecting pressure and added mass effects. It can be observed that when the volumetric fraction is increased in the experiments, the response gets farther away from the line. On the other hand, when superficial velocity is increased, results get closer to the line. This proves that the higher the velocity, the more homogeneous the flow (void fraction is closer to volumetric fraction). The relation between volumetric fraction and void fraction can be summarized by this equation:

$$s \left( \frac{1}{\beta} - 1 \right) = \frac{1}{\varepsilon} - 1 \quad (13)$$

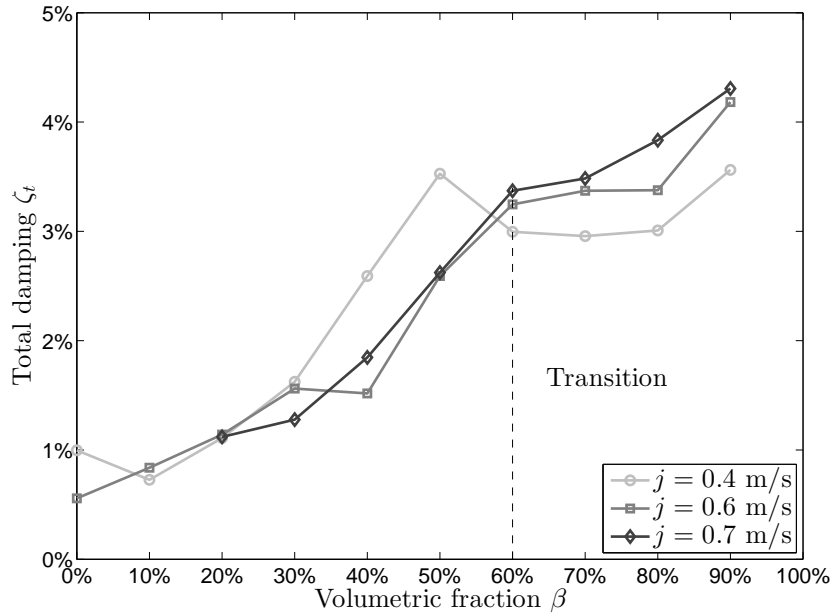


Figure 9. Influence of fluid velocity on total damping.

When  $s$  tends to 1,  $\beta$  becomes closer to  $\varepsilon$ . Physically, in vertical co-current upward flow, gas is faster than liquid due to drag-buoyancy equilibrium. This equilibrium creates a velocity difference that is not much affected by liquid velocity. Therefore, as the liquid velocity gets higher,  $s$  tends to 1. For higher void fractions, flow is intermittent because there is no definite continuous phase. The large diameter of our tube amplifies this effect. Stagnant volumes of water are observed and are subject to sloshing which causes an increase in slip ratio. A superficial velocity of 0.7 m/s is the maximum velocity that can be reached with the current pump.

In the meantime,  $\omega_n$  is a good qualitative indicator of the actual void fraction in the test section, as described in 5.3. The flow conditions at  $\beta = 90\%$  are estimated to correspond approximately to  $\varepsilon = 60\%$ .

## 5.2 Flow patterns

Videos of the flow were taken with a high-speed camera. Selected photographs of each volumetric fraction are shown on 11 for a superficial velocity of 0.7 m/s. Bubbly flow can clearly be observed up to  $\beta = 40\%$ . The breakdown in damping values occurs during the transition to churn regime. Perturbation due to larger bubbles can be made out for  $\beta = 50\% - 60\%$ .

We note that no slug flow regime is observed. That is because the length to diameter ratio is  $L/D_h = 13$ , whereas it should be higher than 20 for slugs to “develop”. This had been observed by [16] who performed void fraction measurements on a very large circular tube of 200 mm inner diameter, and flow conditions comparable to ours. It was also concluded that churn flow was dominant in large pipes for conditions where slug flow exists in smaller pipes. They also reported a phenomenon that can be clearly observed at 80% volumetric fraction. Large Taylor bubbles intermittently perturb a liquid film still filled with many small bubbles. [17] note that those large bubbles can however freely move and deform in three dimensions in the large tube and are thus far from ideal Taylor bubbles.

As reviewed by [18], flow patterns in large circular tubes have been experimented over the years, mostly for horizontal ducts. Flow patterns maps [[19]] were derived and compared reasonably well with theoretical ones [[20]]. Rectangular microchannels and minichannels have also been studied and reviewed thoroughly by [21]. Unfortunately, very little information exists on large rectangular channels. Aspect ratio, surface tension, hydraulic diameter and pressure have an effect on transitions in small (around 5 mm) to micro channels. However, these conclusions may not be verified for large vertical square ducts.

An extensive study of flow pattern transition determination would require additional instrumentation. It is beyond the scope of this study. Our observations of the flow are meant to support damping results and give away the lack of studies in this range of diameter for vertical rectangular ducts.

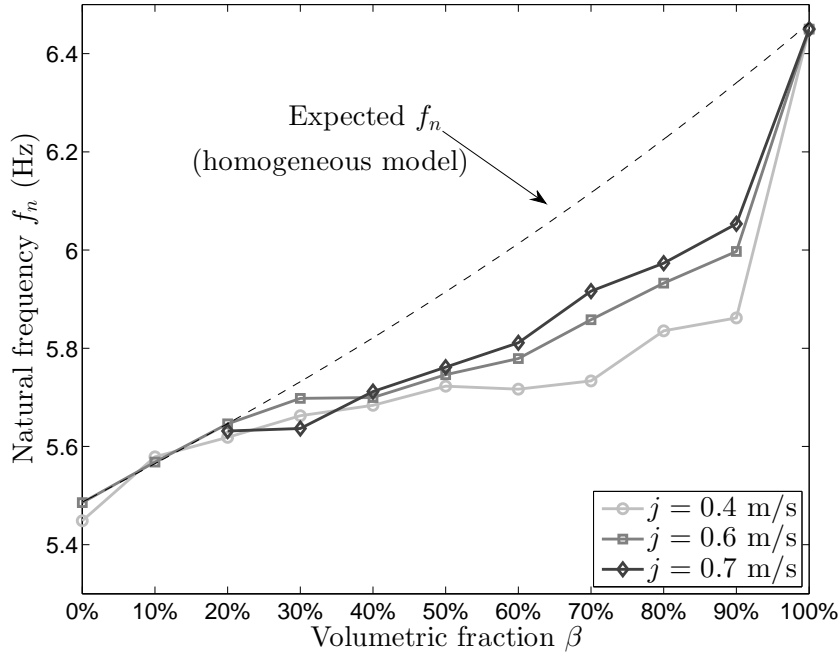


**Figure 10.** Natural frequency of the system for the flow conditions tested. The dotted line represents the expected natural frequency with the homogeneous model, obtained with 14 ( $f_n = \omega_n/2\pi$ ).

### 5.3 Influence of excitation force

The magnitude of excitation force was doubled for  $j = 0.7$  m/s. In order to ensure repeatability with respect to volumetric fraction, natural frequency is used to compare the results. Indeed, if we neglect added mass,  $\omega_n$  is related to hydrodynamic mass  $m_{2\varphi}$  which depends directly on void fraction  $\varepsilon$ :

$$\begin{cases} \omega_n = \sqrt{\frac{k_t}{m_s + m_{2\varphi}}} \\ m_{2\varphi} = (AL + V_{corr})(\varepsilon\rho_g + (1 - \varepsilon)\rho_l) \end{cases} \quad (14)$$

where  $V_{corr}$  is a correction volume that corresponds to the additional volume of vibrating fluid within the flexible tubing. It was determined for  $\varepsilon = 0\%$ .  $\rho_g$  depends on average pressure in the tube. The pressure upstream was found to be below 1.6 bar for all flow conditions. Given the high pressure loss due to the mixer on 3 and the short horizontal length of tubing downstream, the average pressure is close to atmospheric conditions in the oscillating tube. Therefore,  $\rho_g$  was determined at atmospheric conditions, for 23°C. The results are shown on 12.

Clearly, the excitation force has an effect on transition since the two curves separate after the transition. The higher the force, the higher the confinement which is likely to affect flow pattern and the damping values for moderately high void fraction. However, it is interesting to notice that the curves match perfectly before transition, for bubbly flow conditions. This independence of  $\zeta_{2\varphi}$  with respect to  $F_0$  suggests that the damping mechanism can be modeled as a purely velocity dependent mechanism for bubbly flow. In other words,  $\zeta_{2\varphi}$  is independent of excitation amplitude and frequency for bubbly flow. Furthermore, we have depicted the direct dependence of two-phase damping with interface surface area, so we did not expect  $\zeta_{2\varphi}$  to depend on force magnitude. This motivated us to steer the study towards the modeling of two-phase damping mechanism for bubbly flow in 7.

## 6. Gas phase behavior

### 6.1 Video processing

The direct relation between interface surface area and two-phase damping is not sufficient to explain the two-phase damping mechanism. We suspect that relative motion between the phases induces dissipation, through the work of the forces exerting on the bubbles.

We used a high-speed camera at 1000 fps to characterize the gas phase motion for bubbly flow within the oscillating structure. The objective is to correlate the gas phase motion to the damping values measured. To do so,  $\beta$  should be sufficiently high (for lower volumetric fraction, two-phase

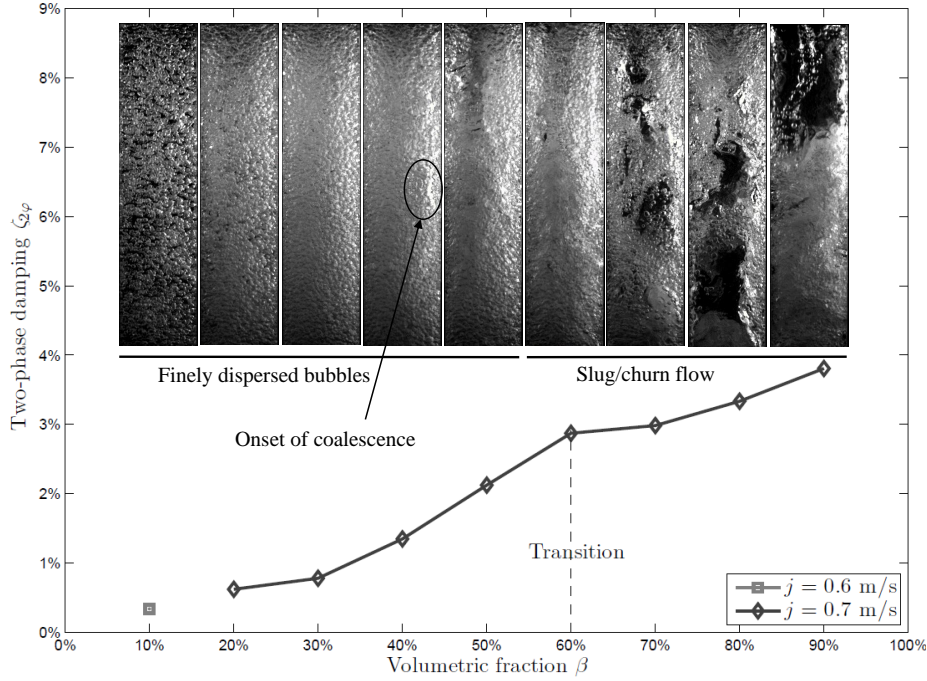


Figure 11. Flow patterns.

damping would be too small to be measured accurately). Unfortunately, the higher the void fraction, the harder the characterization. For instance, [22] presented an accurate measurement of the flow field with bubbles using a combined PIV/shadowgraphy technique. However, the local void fraction around the cluster of bubbles does not exceed 2.5%. The challenge in our case is that many inter-bubble motions were observed, including overlapping. For this reason, individual tracking of the bubbles with image segmentation techniques is laborious.

Therefore, we resorted to a global tracking of the gas phase motion. The method consists in selecting a thumbnail of an image at instant  $t$ , and looking for the same thumbnail in the next image at time  $t + \Delta t$ . We note  $f(t)$  the full image matrices taken with the high speed camera, of constant size  $(M, N)$  at instant  $t$ . The indices of the thumbnail position are noted  $(i(t), j(t))$ . The new coordinates indices  $(i(t + \Delta t), j(t + \Delta t))$  are calculated in order to minimize the Mean Square Error (MSE), expressed as:

$$MSE = \sum_{\substack{M/2 < I \leq M/2 \\ -N/2 < J \leq N/2}} [f(i(t) + I, j(t) + J) - f(i(t + \Delta t) + I, j(t + \Delta t) + J)]^2 \quad (15)$$

The high frame rate was set so that the minimization could be performed in a region of pixels close to the original thumbnail. The thumbnail should of course be initialized in the middle of the gas phase. At each time step, the new thumbnail is used to look for the next one. This evolution of  $f(i(t), j(t))$  tends to average the inter-bubble motion and gives a good representation of the bulk gas phase motion.

The resolution is around 1 pixel = 0.2 mm. While very simple and robust, the drawback of this technique is that its accuracy can only be appreciated qualitatively.

On 13, one can directly observe the gas phase relative motion with respect to the structure. The images are shown in the tube reference frame. On the first image, the test section is accelerating towards the left, and the gas column is already compressed on the left wall of the tube. This suggests that bubbles are in phase lead with respect to the structure. On the second frame, the tube reaches a zero velocity point, so the gas phase is uniformly dispersed, before being compressed on the right. Notice the white rectangle, standing for the tracked thumbnail. It has moved not only in the transverse direction but also upward. Indeed, upward co-current air-water mixtures are studied.

## 6.2 Characterization of gas phase motion

Experiments for three volumetric fractions  $\beta = 5, 10$  and  $15\%$ , at constant superficial velocity  $j = 0.6$  m/s. Since the shape of the thumbnail does not change, only one point of its coordinates  $(i(t), j(t))$  is required to track the bulk gas phase motion with respect to time.  $i(t)$  and  $j(t)$  correspond

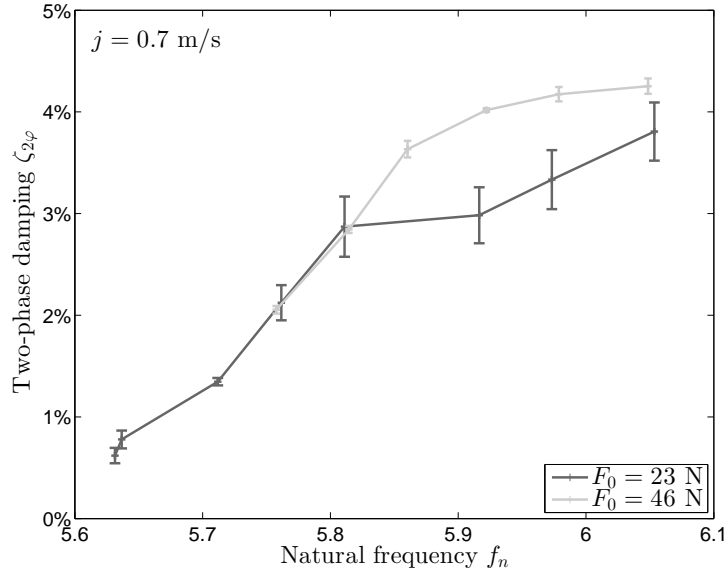


**Figure 12.** Influence of force magnitude. Natural frequency is taken as reference for comparison, since it represents the actual void fraction more accurately (cf. 10). Note that  $\zeta_{2\phi}$  is independent of  $F_0$  for bubbly flow.

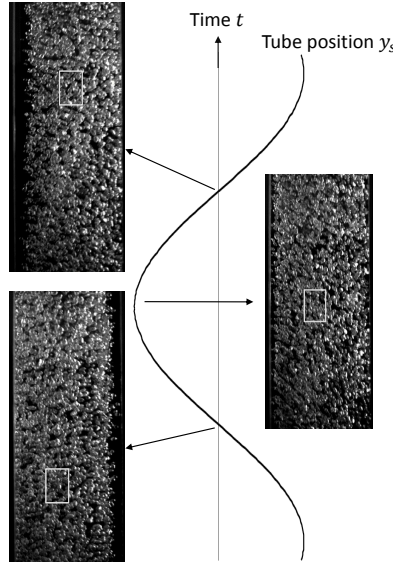


**Figure 13.** Relative motion of the gas phase.

respectively to the vertical and transverse motions. Vertical relative velocity with respect to the liquid  $u_{gz} - u_{lz}$ , ranges from 0.22 to 0.28 m/s. This is around the expected value of 0.25 m/s (given by the difference between buoyancy and drag force on the bubbles). Those values give a slip ratio  $s$  of approximately 1.5. The three corresponding void fractions  $\varepsilon$  are thus roughly 3, 7 and 11%.

A typical graph of transverse relative motion of the bubbles is shown on 14. The signal is the combination of a sine wave and a linear deviation, meaning the tracking rectangle is oscillating while drifting towards one side of the tube. Note that only bubbles close to the front window are observed. We attribute the drift behavior to a swirling motion of the bubbles. When the structure is oscillating, a radial instability is onset (the swirling motion was not observed for the tube at rest). When bubbles come into contact with the side walls, they tend to slide in a preferential direction instead of simply bouncing back and most likely coalesce with other bubbles. This is attested by the photographs in 13 where structural oscillations do not seem to prematurely onset the formation of larger bubbles. A similar behavior had been reported by [11]. When their clamped-clamped tube was released to measure the free vibrations, they observed elliptical motion instead of oscillations in a plane. This phenomenon was attributed to the cylindrical shape of the tube causing swirling. Our observations suggest that swirling is generated by tube oscillations only, and not by tube geometry. The swirling velocities on the side wall were around 0.05 m/s (slope of the dashed line on 14), which is negligible compared to up to 1 m/s for structure peak velocity. Thus, the swirling motion is not dissipative.

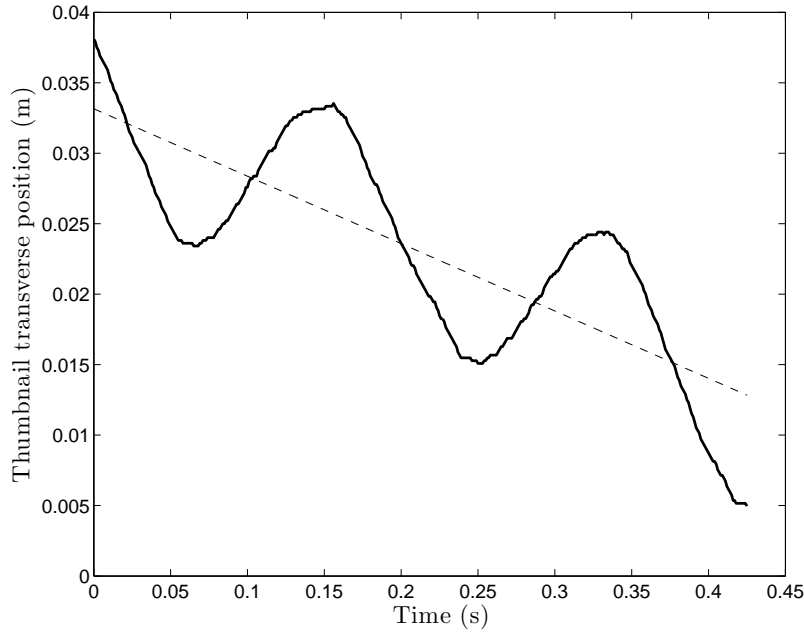


**Figure 14.** Typical unfiltered transverse position of the tracking rectangle in time. It represents the gas phase motion on the front tube wall. The linear deviation is attributed to a global swirling motion of the bubbles.

However, it prevents coalescence of the bubbles, keeping a constant interface surface area. It could explain why tube oscillations do not seem to affect flow pattern transitions.

Therefore, only the harmonic motion of the gas phase is extracted. The tube amplitude is noted  $Y_s$  and the relative amplitude of motion of the gas phase with respect to the tube is  $Y_{b|s}$ . The corresponding time-dependent motions are noted  $y_s$  and  $y_{b|s}$ . Fig. 15 shows the different movements of the system involved. Note that the gas phase is in phase lead with respect to the structure.

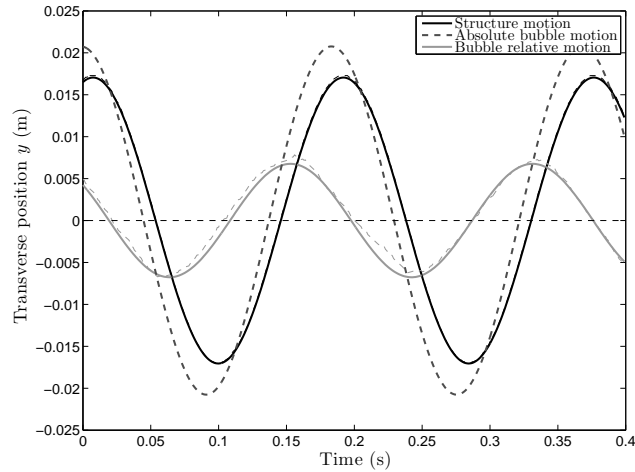


**Figure 15.** Different movements of the system involved. Light dashed lines are the the raw signals extracted from the videos, and solid lines are the corresponding sinusoidal fits.

### 6.3 Amplitude of motion of the gas phase

The relative amplitude  $Y_{b|s}$  was extracted for several excitation amplitudes.  $Y_s$  was varied by changing the frequency close to the natural frequency of the system for a given void fraction. Since the peak of resonance is very well defined, the excitation frequency can be considered constant at  $33.75 \pm 1.5$  rad/s ( $6 \pm 0.23$  Hz) over all our experiments. Results are shown on 16.  $Y_{b|s}/Y_s$  represents the gain of the gas in terms of amplitude. For a constant excitation amplitude, the gain of the gas tends to decrease when void fraction increases. This is in accordance with the drag relations that take into account the effect of void fraction [e.g. [23], [24]]. Indeed, it is well-established that  $C_D$  increases dramatically with  $\varepsilon$  through confinement, therefore limiting the transverse amplitude.

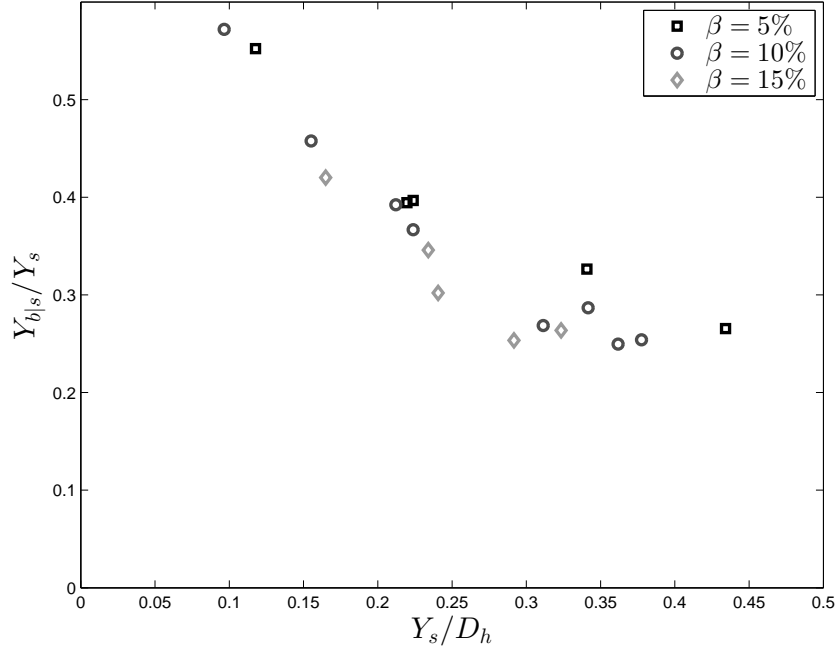


Figure 16. Relative amplitude of the gas phase with respect to the structure.

For high  $Y_s$ , the gain seems to reach an asymptote. As explicitly shown in 7.1, important shape deformation for high excitation amplitudes cause an increase of the drag force on the bubbles. Also, it is well established that wall proximity causes a similar effect on the drag force [25]. In this case, the tube walls are moving and thus represent a physical barrier that cannot be crossed by the bubbles, leading to an important confinement effect. All these effects contribute to the existence of the limit cycle.

The relative motion can not be related to two-phase damping values without the forces on the bubbles. Therefore, a simple model has to be analytically derived.

## 7. Analytical model

We propose a simple model of a bubble in an oscillating structure subjected to internal two-phase flow. This sections aims at testing existing correlations and implement them in the model under certain hypotheses, to assess the extent to which the two-phase damping can be reproduced. Based on our observations, the transverse relative motion of the gas phase will be the main output of the calculations to explain damping, through the work of the forces exerting on the bubbles.

### 7.1 Equation of motion

We consider a deformable bubble of equivalent diameter  $a$ . It is immersed in an oscillating structure filled with water, as illustrated by 17. The bubble has the properties of a confined bubble in two-phase flow, of given volumetric fraction and superficial velocity. Thus, its movement is representative of the gas phase motion.

We note  $\vec{u}_b$  the relative velocity of the bubble with respect to the fluid:

$$\vec{u}_b = \vec{u}_g - \vec{u}_l \quad (16)$$

We assume that bubbles do not have influence on the liquid. Thus, the liquid undergoes a solid body motion with the structure. Therefore:

$$\vec{u}_l = (-Y_s \omega \sin(\omega t), u_{lz}) \quad (17)$$

where  $u_{lz}$  is a function of  $j$  and  $\varepsilon$ , the void fraction still being calculated based on volumetric fraction and slip ratio of the bubble.

The 2D equation of motion of the bubble takes the form:

$$m \frac{d\vec{u}_b}{dt} = \vec{F}_B + \vec{F}_D + \vec{F}_M + \vec{F}_I \quad (18)$$

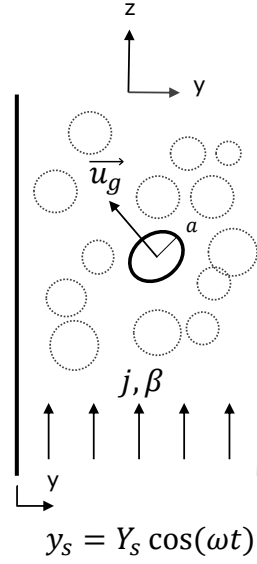


**Figure 17.** Schematic of the bubble model in an oscillating structure subjected to two-phase flow.

where  $\vec{F}_B$  is the buoyancy force:

$$\vec{F}_B = \frac{4}{3}\pi a^3 \Delta\rho g \vec{z} \quad (19)$$

$\vec{F}_D$  is the drag force, based on bubble relative velocity:

$$\vec{F}_D = -\frac{1}{2}\pi a^2 \rho_l C_D u_b \vec{u}_b \quad (20)$$

We calculate the drag coefficient using a relation by [26]. It is valid for up to  $Re = 300$ , and takes the effect of void fraction into account:

$$C_D = \frac{16}{Re} \left( 1 + \frac{2 \left( \frac{2 + 3\mu^*}{2 + 2\mu^*} \right)^2}{1 + \frac{Re_c}{Re}} \right) \frac{1 - \varepsilon}{(1 - \varepsilon^{1/3})^3} \left[ \frac{P_1 + \mu^* P_2}{P_3 + \mu^* P_4} \right] G(\chi)$$

with :

$$P_1 = 4 + 6\varepsilon^{5/3} \quad (21)$$

$$P_2 = 6 - 6\varepsilon^{5/3}$$

$$P_3 = 4 + 6\varepsilon^{1/3} + 6\varepsilon^{2/3} + \varepsilon$$

$$P_4 = 4 + 3\varepsilon^{1/3} - 3\varepsilon^{2/3} - 4\varepsilon$$

$$Re_c = 33 + 8600\varepsilon^{2/3}$$

$$G(\chi) = \frac{1}{3}\chi^{4/3}(\chi^2 - 1)^{3/2} \frac{\sqrt{\chi^2 - 1} - (2 - \chi^2)\sec^{-1}\chi}{(\chi^2 \sec^{-1}\chi - \sqrt{\chi^2 - 1})^2}$$

The oblateness  $\chi$  of the bubble is calculated with a terminal velocity correlation by [27] (first-order term only):

$$\chi = 1 + \frac{9}{64} We \quad (22)$$

where the Weber number  $We$  is defined as:

$$We = \frac{2a\rho_l u_b^2}{\sigma} \quad (23)$$

The relation of 22 is valid for a single bubble rising in stagnant liquid, so its application is questionable in our case. For instance, oblateness tends to increase with void fraction ([28], [29]). However, our observations show that bubbles change shape depending on structure position, and so that velocity is the major parameter controlling the bubble deformations.

$\vec{F}_M$  is the added mass force:

$$\vec{F}_M = -\frac{4}{3}\pi a^3 \rho_l C_M \frac{d\vec{u}_b}{dt} \quad (24)$$

where  $C_M$  is the added mass coefficient. A few studies propose the effect of void fraction on the added mass of a bubble. See for instance the works by [30] or [31]. However, added mass could increase or decrease with  $\varepsilon$  depending on certain hypotheses. A more recent study by [32] proposes a new semi-empirical correlation based on potential flow theory for random clouds of bubbles. It appears that  $C_M$  weakly increases with  $\varepsilon$ . Therefore, we will simply use the added mass coefficient  $C_M = 0.5$  of an isolated sphere as a first approximation.

Finally, the bubble undergoes an inertia force  $\vec{F}_I$  because of the pressure gradient caused by the accelerating tube on the water, in the transverse direction. This force can be expressed as:

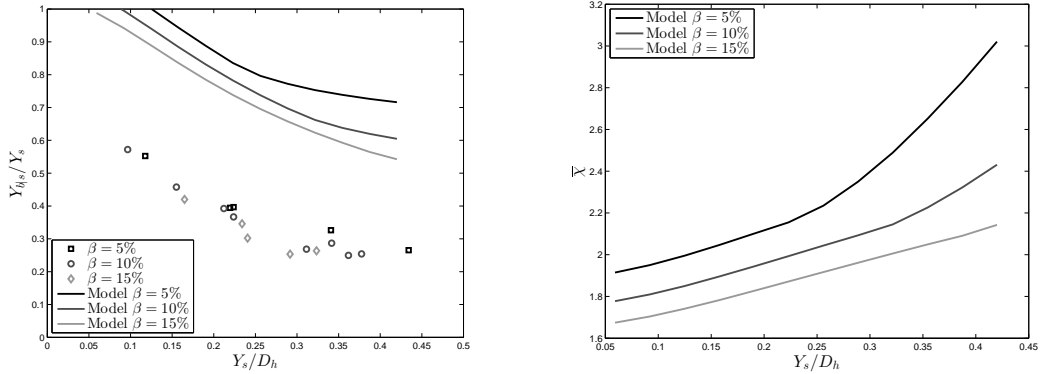
$$\vec{F}_I = \frac{4}{3}\pi a^3 \rho_l \ddot{y}_s \quad (25)$$

To sum up, the only input parameters for the model are  $a$ ,  $j$  and  $\beta$ . The motion of the bubble is governed by its added mass and fluid viscosity. Thus, it has no mass nor rigidity, as modeled by [6].

## 7.2 Transverse amplitude

A few images of the oscillating structure at different instants were segmented in order to have an estimate of the bubble sizes and shapes, for  $Y_s/D_h = 0.22$ . The bubble radii  $a$  were found to range within [1.2, 2] mm and oblateness  $\chi$  within [1.2, 1.9], assuming a revolution ellipsoid. For the same conditions and  $a = 1.4$ , the model predicts  $\chi$  up to 2.3, which seems reasonable considering the fact that the correlation we use do not take the effect of acceleration into account.

The predicted bubble relative amplitude  $Y_{b|s}$  is presented on 18(a). The model tends to over-predict the amplitude by a factor 2. Thus, some effects have obviously been overlooked. Still, the



(a) Comparison between model and experimental values for gas phase transverse amplitude.

(b) Mean oblateness

Figure 18. Analytical model results solving eq. (18-25)

trend seems very well respected. The limit cycle reached is mostly due to the oblateness of the bubbles, as attested by 18(b).

## 7.3 Dissipated energy

It is also useful to compare the model directly to the damping values measured for bubbly flow. We decided to compare the energy dissipated by the two-phase damping force  $F_{2\varphi}$  over one cycle of oscillation:

$$E_{2\varphi} = \int_0^{2\pi/\omega} F_{2\varphi} \frac{dy_s}{dt} dt = \int_0^{2\pi/\omega} c_{2\varphi} y_s^2 dt = \pi c_{2\varphi} \omega Y_s^2 \quad (26)$$

This energy has to be compared with that dissipated by the work of the forces applied on the bubbles. We are only interested in the projection in the  $y$  direction of these forces since we try to explain two-phase damping with transverse motion of bubbles. The buoyancy force is vertical and as such is not accounted for. Added mass and inertia forces are purely inertial, hence they do not work over one cycle. Only the work of the drag force projected on the  $y$ -axis is contributing, and can be written as:

$$W_D = N_b \int_0^{2\pi/\omega} \vec{F}_D \cdot \vec{y} \frac{dy_{b|s}}{dt} dt \quad (27)$$

$N_b$  stands for the number of bubbles in the test section. It is calculated based on the void fraction:

$$N_b = \frac{\varepsilon AL}{\frac{4}{3}\pi a^3} \quad (28)$$

This equation is valid only for bubbly flow (up to  $\beta \approx 50\%$  experimentally), so no effect of coalescence is considered. The void fraction depends on volumetric fraction and slip ratio (previously defined in the  $z$  direction). Comparison between the model and experiments is shown on 19.

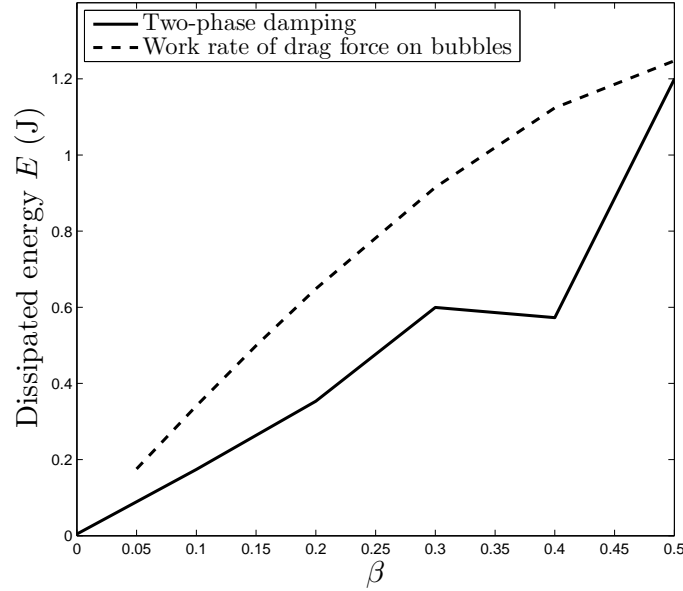


**Figure 19.** Energy dissipated over one oscillation cycle. – : by two-phase damping using 26; - - : calculated with analytical model using 27. Only the power of bubble drag forces is significant in the model. Calculations are presented for structure amplitude  $Y_s = 18.8$  mm, superficial velocity  $j = 0.6$  m/s and bubble radius  $a = 1.4$  mm.

The model compares fairly well with two-phase damping in terms of dissipated energy. It is odd to have a good agreement for the energy, and a poor one for relative amplitude of the bubbles as reported in 7.2. Assuming that the drag relation is correct, we believe this is due to the fact that we measured relative amplitude of the gas phase with respect to the structure, and not the liquid, as underlined in the next section.

#### 7.4 Model calibration with glycerin experiments

Changing the Reynolds number is a good way to test the validity of the model for other flow conditions. Other videos were taken with a stagnant glycerin solution ( $j = 0$ ). Glycerin density is 1.21. Its viscosity was tested with a rheometer and was found to be of 0.163 Pa.s at 22°C. Single bubbles were injected with a needle. The Reynolds numbers based on bubble relative velocities were below 3. Using segmentation imaging techniques, we were able to measure bubble radii, transverse amplitude and vertical terminal velocity (cf. 20(a) and 20(b)).

The scatter in the data is explained by the fact that we do not control the bubble radius. This is why the points were gathered in several radius categories, thus collapsing the data. The structural transverse amplitude does not have a strong effect on  $Y_{b|s}$ . Given the low Weber numbers of the experiments, the bubbles hardly deform ( $\chi \approx 1$ ). Hence, no additional drag is induced. Also note that the graphs are basically identical on their respective scale. Experimentally, the bubbles would rise in glycerin in a straight line due to the very low Reynolds number (two path instabilities occur at higher  $Re$ , as reported extensively in the literature, *e.g.* [33] and [34]). Hence, at this range of  $Re$ , transverse migration is only due to tube motion and depends directly on bubble radius, as attested by 21. The figure summarizes the twenty-five experiments in stagnant glycerin. Since all the points collapse on a straight line, the relative amplitude of the bubble is only a function of its radius. However, two bubbles with different radii have different terminal velocities in the  $z$  direction, as attested by Fig. 19(b). This confirms that no coupling exists between the  $y$  and  $z$  directions in this case.

Contrary to 7.2, the agreement between the model and experiments on 20 is very good, for both  $U_t$  and  $Y_{b|s}$ . This suggests that considering the relative amplitude with respect to the structure or the

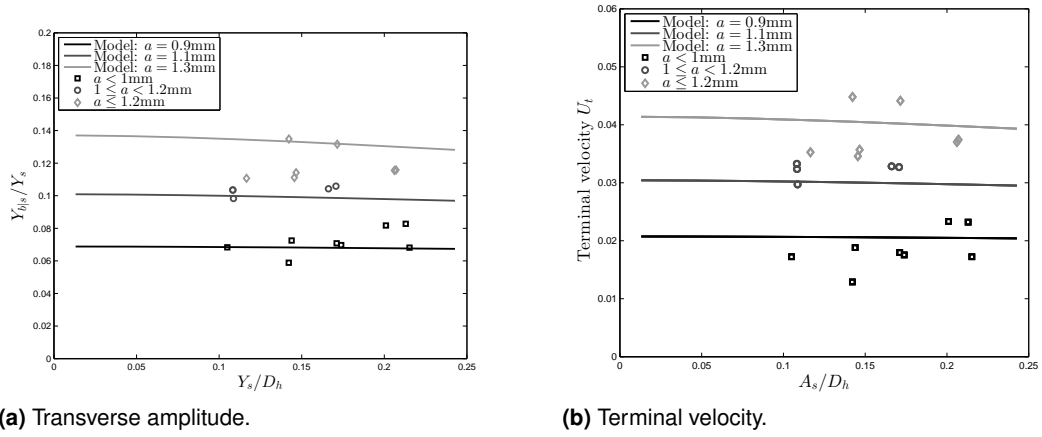


**Figure 20.** Comparison between model and experiments with single bubbles rising in stagnant glycerin.

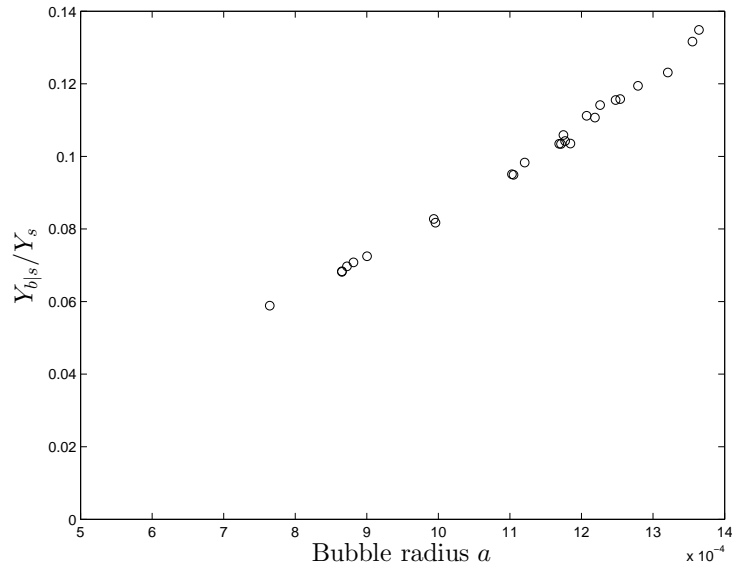


**Figure 21.** Gain of the bubbles as a function of bubble radius, in stagnant glycerin (experimental).

liquid is the same. Hence, assuming solid body motion for the liquid is correct in this case. The poor agreement reported before for air-water mixture experiments may be caused by a recirculation of water around bubbles or a wrong drag coefficient given the bubbles' high Reynolds number. Indeed, the higher the void fraction, the more important the recirculation to fill the space between the moving bubbles. This interstitial flow would affect both drag on bubbles and relative velocity.

Furthermore, we stated in 6.2 that structural oscillation did not seem to onset bubble coalescence. The nature of the liquid film between bubbles would control their coalescence/break-up conditions [[35]]. The local gas-liquid interaction due to the relative bubble motion is given by pseudo-turbulence theory but is beyond the scope of this study. Bubble-induced liquid agitation was modeled [e.g. [36] and [26]] and characterized experimentally at moderate void fractions [[37] and [38]]. Information on local interstitial velocity in an oscillating structure with gas bubbles would allow to model turbulence forces on bubbles as well as lift forces (through information on local vorticity) which were neglected in the present model. This effect is important even for two-phase flow in tubes at rest for void fractions larger than 2% [[29]]. Thus, it is likely that structural oscillations cause additional pseudo-turbulence when inducing the relative motion of the gas phase. Characterizing this phenomenon might help to understand the two-phase damping mechanism more thoroughly.

## 8. Conclusion

In this paper, a new test section offering control over the excitation parameters in order to determine two-phase damping experimentally was presented. Observations as well as processing of high-speed videos gave novel information on the gas phase motion, especially on its relative motion with respect to the structure. A simple analytical model fed with correlations was derived. Although not

entirely complete, the model gives useful information on the physical dissipative mechanism. It also underlines the missing information to catch the full nature of the phenomenon. We suspect that the latter lies in the complexity of the liquid phase motion. So far, the following conclusions and perspectives can be brought out:

- (i) Two-phase damping can reach 3% in this square 76.2 mm tube. It is fairly proportional to void fraction, until a change in slope at transition between bubbly and churn flow regime occurs.
- (ii) The frequency response function of the tube subjected to internal two-phase flow confirms that two-phase damping is a viscous damping (velocity dependent) mechanism. This is supported by the fact that  $\zeta_{2\varphi}$  seems independent of the excitation force magnitude  $F_0$  for bubbly flow. For higher void fraction, the mechanism is different. We suspect that energy is extracted by sloshed liquid phase within the continuous gas phase. Damping is affected by the stochastic nature of the flow at this regime, causing an increase of standard deviation in the results.
- (iii) There is definite relative motion of the gas phase with respect to the liquid for bubbly flow. The bubbles have a bulk body motion due to the tube oscillations, and are in phase lead with respect to the structure. The oscillations seem combined with a swirling motion. It is not very dissipative but helps to prevent a premature coalescence of the bubbles, keeping a maximum interface surface area prompt to transfer energy between the phases and the structure.
- (iv) For bubbly flow, the power dissipated by two-phase damping is equivalent to that dissipated by the drag forces on the bubbles. However, the discrepancy between bubble amplitudes predicted by the model and those measured suggests a complex interstitial liquid flow between the bubbles under tube oscillations, affecting both drag and relative velocity. It seems like even though two-phase damping is observed on a large scale, small scale effects cannot be overlooked for  $\zeta_{2\varphi}$  to be accurately modeled.

## Acknowledgments

This work was sponsored by the Natural Sciences and Engineering Research Council, Babcock & Wilcox Canada and Atomic Energy of Canada Ltd., through the BWC/AECL/NSERC research chair in fluid-structure interactions.

## References

- [1] M. J. Pettigrew, C. E. Taylor, Fluidelastic instability of heat exchanger tube bundles; review and design recommendations, *Journal of Pressure Vessel Technology* 113 (2).
- [2] D. S. Weaver, J. A. Fitzpatrick, A review of cross-flow induced vibrations in heat exchanger tube arrays, *Journal of Fluids and Structures* 2 (1) (1988) 73 – 93. doi:10.1016/S0889-9746(88)90137-5.
- [3] M. K. Au-Yang, S. S. Chen, M. P. Païdoussis, M. J. Pettigrew, D. S. Weaver, S. Ziada, Flow-induced vibrations in power and process plant components - progress and prospects, *Journal of Pressure Vessel Technology* 122 (3) (2000) 339–348.
- [4] L. N. Carlucci, Damping and hydrodynamic mass of a cylinder in simulated two-phase flow, *Journal of Mechanical Design* 102 (3) (1980) 597–602.
- [5] L. N. Carlucci, J. D. Brown, Experimental studies of damping and hydrodynamic mass of a cylinder in confined two-phase flow, *Journal of Vibration Acoustics Stress and Reliability in Design* 105 (1983) 83.
- [6] F. Hara, O. Kohgo, Analytical model for evaluating added mass and damping of a vibrating circular rod in two-phase fluid, in: *Transactions of the 8. international conference on structural mechanics in reactor technology*. Vol. F1 and F2, 1985.
- [7] T. Uchiyama, Numerical prediction of added mass and damping for a cylinder oscillating in confined incompressible gas–liquid two-phase mixture, *Nuclear engineering and design* 222 (1) (2003) 68–78.
- [8] M. J. Pettigrew, C. E. Taylor, Damping of heat exchanger tubes in two-phase flow: review and design guidelines, *Journal of pressure vessel technology* 126 (4) (2004) 523–533.
- [9] A. Gravelle, A. Ross, M. J. Pettigrew, N. W. Mureithi, Damping of tubes due to internal two-phase flow, *Journal of Fluids and Structures* 23 (3) (2007) 447 – 462. doi:http://dx.doi.org/10.1016/j.jfluidstructs.2006.09.008.

- [10] C. Béguin, J. Wehbe, A. Ross, M. J. Pettigrew, N. W. Mureithi, Influence of viscosity, density and surface tension on two-phase damping, in: ASME 2009 Pressure Vessels and Piping Conference, American Society of Mechanical Engineers, 2009, pp. 247–257.
- [11] C. Béguin, F. Anscutter, A. Ross, M. J. Pettigrew, N. W. Mureithi, Two-phase damping and interface surface area in tubes with vertical internal flow, *Journal of Fluids and Structures* 25 (1) (2009) 178–204.
- [12] J. G. Collier, J. R. Thome, *Convective boiling and condensation*, Oxford University Press, 1994.
- [13] A. Van Beek, *Advanced engineering design: lifetime performance and reliability*, Vol. 1, 2006.
- [14] J. P. Den Hartog, *Mechanical vibrations*, Dover Publications, 1956.
- [15] H. Olsson, K. J. Åström, C. Canudas de Wit, M. Gäfvert, P. Lischinsky, Friction models and friction compensation, *European journal of control* 4 (3) (1998) 176–195.
- [16] A. Ohnuki, H. Akimoto, Experimental study on transition of flow pattern and phase distribution in upward air–water two-phase flow along a large vertical pipe, *International journal of multiphase flow* 26 (3) (2000) 367–386.
- [17] H.-M. Prasser, M. Beyer, A. Böttger, H. Carl, D. Lucas, A. Schaffrath, P. Schutz, F.-P. Weiss, J. Zschau, Influence of the pipe diameter on the structure of the gas-liquid interface in a vertical two-phase pipe flow, *Nuclear technology* 152 (1) (2005) 3–22.
- [18] J. W. Coleman, S. Garimella, Characterization of two-phase flow patterns in small diameter round and rectangular tubes, *International Journal of Heat and Mass Transfer* 42 (15) (1999) 2869–2881.
- [19] J. M. Mandhane, G. A. Gregory, K. Aziz, A flow pattern map for gas—liquid flow in horizontal pipes, *International Journal of Multiphase Flow* 1 (4) (1974) 537–553.
- [20] Y. Taitel, A. E. Dukler, A model for predicting flow regime transitions in horizontal and near horizontal gas-liquid flow, *AIChE Journal* 22 (1) (1976) 47–55.
- [21] L. Cheng, G. Ribatski, J. R. Thome, Two-phase flow patterns and flow-pattern maps: fundamentals and applications, *Applied Mechanics Reviews* 61 (5) (2008) 050802.
- [22] R. Lindken, W. Merzkirch, A novel PIV technique for measurements in multiphase flows and its application to two-phase bubbly flows, *Experiments in fluids* 33 (6) (2002) 814–825.
- [23] M. Ishii, N. Zuber, Drag coefficient and relative velocity in bubbly, droplet or particulate flows, *AIChE Journal* 25 (5) (1979) 843–855.
- [24] N. Zuber, J. Hench, Steady state and transient void fraction of bubbling systems and their operating limits (part i, steady state operation), General Electric Report 62GL100.
- [25] F. Takemura, S. Takagi, J. Magnaudet, Y. Matsumoto, Drag and lift forces on a bubble rising near a vertical wall in a viscous liquid, *Journal of Fluid Mechanics* 461 (2002) 277–300.
- [26] C. Béguin, *Modélisation des écoulements diphasiques: amortissement, forces interfaciales et turbulence diphasique.*, Ph.D. thesis, École Polytechnique de Montréal (2010).
- [27] V. I. Kushch, A. S. Sangani, P. D. M. Spelt, D. L. Koch, Finite-weber-number motion of bubbles through a nearly inviscid liquid, *Journal of Fluid Mechanics* 460 (2002) 241–280.
- [28] P. C. Duineveld, The rise velocity and shape of bubbles in pure water at high reynolds number, *Journal of Fluid Mechanics* 292 (1995) 325–332.
- [29] V. Roig, A. Larue de Tournemine, Measurement of interstitial velocity of homogeneous bubbly flows at low to moderate void fraction, *Journal of Fluid Mechanics* 572 (2007) 87–110.
- [30] N. Zuber, On the dispersed two-phase flow in the laminar flow regime, *Chemical Engineering Science* 19 (11) (1964) 897–917.
- [31] X. Cai, G. B. Wallis, A more general cell model for added mass in two-phase flow, *Chemical engineering science* 49 (10) (1994) 1631–1638.
- [32] C. Béguin, E. Pelletier, S. Étienne, Void fraction effect on added mass in bubbly flow, in: ASME 2014 Pressure Vessels and Piping Conference, American Society of Mechanical Engineers, 2014.
- [33] A. Tomiyama, G. P. Celata, S. Hosokawa, S. Yoshida, Terminal velocity of single bubbles in surface tension force dominant regime, *International Journal of Multiphase Flow* 28 (9) (2002) 1497–1519.

- [34] G. Mougin, J. Magnaudet, Path instability of a rising bubble, *Physical review letters* 88 (1) (2001) 014502.
- [35] M. M. Razzaque, A. Afacan, S. Liu, K. Nandakumar, J. H. Masliyah, R. S. Sanders, Bubble size in coalescence dominant regime of turbulent air–water flow through horizontal pipes, *International journal of multiphase flow* 29 (9) (2003) 1451–1471.
- [36] S. E. Elghobashi, T. W. Abou-Arab, A two-equation turbulence model for two-phase flows, *Physics of Fluids (1958-1988)* 26 (4) (1983) 931–938.
- [37] M. Lance, J. Bataille, Turbulence in the liquid phase of a uniform bubbly air–water flow, *Journal of Fluid Mechanics* 222 (1991) 95–118.
- [38] G. Riboux, F. Risso, D. Legendre, Experimental characterization of the agitation generated by bubbles rising at high reynolds number, *Journal of Fluid Mechanics* 643 (2010) 509–539.